XL CILAMCE
IBERO-LATIN AMERICAN CONGRESS ON COMPUTATIONAL METHODS IN ENGINEERING
NOVEMBER 11-14, 2019
Praiamar Natal Hotel & Convention Natal, RN-BRAZIL

FINITE ELEMENT NUMERICAL IMPLEMENTATION OF A MICROMECHANICS-BASED VISCOELASTIC MODEL FOR FRACTURED GEOMATERIALS

Ricardo Haniel Moran Ramirez
Cassio B. de Aguiar
Eduardo Bittencourt
Samir Maghous
ricardo.moran@ufrgs.br
cassio.barros.aguiar@gmail.com
eduardo.bittencourt@ufrgs.br
samir.maghous@ufrgs.br
Universidade Federal do Rio Grande do Sul
99 Osvaldo Aranha Av. - Historic Centre, 90035-190, Porto Alegre, Rio Grande do Sul, Brazil

Abstract. The constitutive behavior of geomaterials is generally affected by the presence at different scales of discontinuity surfaces with different sizes and orientations. According to their mechanical behavior, such discontinuities can be distinguished as cracks or fractures. Fractures are interfaces that can transmit normal and tangential stresses, whereas cracks are discontinuities without stress transfer. As far as the formulation of the behavior of materials with isotropic distribution of micro-cracks or fractures is concerned, previous works had essentially focused on their instantaneous response induced by structural loading. Few research works have addressed time-dependent (delayed) behavior of such materials. The present contribution describes the formulation and computational implementation of a micromechanics-based modeling for viscoelastic micro-fractured media. The effective viscoelastic properties are assessed by implementing a reasoning based on linear homogenization schemes (Mori-Tanaka) together with the correspondence principle for non-aging viscoelastic materials. It is shown that the homogenized viscoelastic behavior can be described by means of a generalized Maxwell rheological model. The computational implementation is developed within the finite element framework to analyze the delayed behavior of geomaterials with presence of isotropically distributed micro-fractures under plane strain conditions. Several examples of applications are presented with the aim to illustrate the performances of the finite element modeling. The accuracy of the approach is also assessed by comparing the numerical predictions with analytical solutions.

Keywords: Fracture, Micromechanics, Viscoelasticity, Finite element

1 Introduction

One of the most common causes of material degradation in civil engineering structures is the presence of discontinuity surfaces, which can appear in certain zones with different sizes and orientations. The existence of these small thickness regions increases the risk of mechanical properties deterioration during the service life of structures because of a significative reduction of stiffness, strength, ductility and a serious increase of permeability. From a mechanical behavior perspective of materials, there are two principal types of discontinuities: cracks and fractures. Essentially, cracks have no stress transfer between faces, whereas fractures can transfer normal and tangential stress. Consequently, a medium can be considered as cracked or fractured depending on the characteristics of its discontinuities.

Geomaterials under long-term loading present two types of response: instantaneous and delayed. The instantaneous response of geomaterials have been object of research over the years, but less attention has been given to delayed response in fractured mediums. Recently, there was an increase in research works on time-dependent response that simultaneously address fracture mechanics and viscoelasticity. Such tendency reveals positive even more when it is known that delayed behavior has an important impact on stress-strain response of geomaterials. In order to study and characterize that behavior, several mathematical models have been analytically formulated. Among these models, there exist those based on a micromechanics framework.

Some important micromechanics-based research works that considered delayed behavior were developed by Nguyen [1] and Nguyen et al. [2]. These researchers formulated a micromechanics-based model for a viscoelastic medium where the heterogeneities were considered as cracks. However, as mentioned above, there are no stress transfer in this type of discontinuities. Subsequently, Nguyen´s analysis was extended by Aguiar and Maghous [3], who added the fracture behavior studied. In this context, the overall aim of this paper is to show the computational implementation of the micromechanics-based viscoelastic model formulated by Aguiar and Maghous [3] considering an isotropic distribution of micro-fractures in geomaterials.

The paper content is organized as follows. Section 2 presents succinctly the theoretical formulation for the homogenized viscoelastic behavior of fractured mediums considering an isotropic distribution of micro-fractures. Section 3 describes the algorithm used for time discretization of the viscoelastic model. Section 4 aims to verify the implementation code by presenting several examples of application where the accuracy of the numerical responses is assessed through comparison with the corresponding analytical solutions. Finally, section 5 illustrates the predictive capabilities of the computational tool by analyzing the delayed response of complex geo-structures.

2 Formulation of the homogenized viscoelastic model

As mentioned above, Aguiar and Maghous [3] formulated the homogenized viscoelastic properties for a fractured medium. This approach is based on prior research works developed within the framework of elastic fractured mediums (Maghous et al. [4]) and the elastic-viscoelastic correspondence principle in the context of non-aging materials. There are two principal steps in order to formulate the macroscopic viscoelastic properties: in the first place, it is necessary to formulate the overall elastic properties of the medium taking advantage of linear homogenization schemes. The second step is to associate the elastic-viscoelastic correspondence principle (Le [5]) with a specific procedure to determinate the inverse Laplace-Carson transform of a function.

Since paper focus is the display of the computational implementation of the viscoelastic model, only the formulation of the homogenized viscoelastic properties in a medium with isotropically distributed fractures will be shown below in a concise way. The formulation of the elastic properties in a fracture medium, the complete procedure of inverse Laplace-Carson transform and other basic concepts of the theoretical model can be found in the research work of Aguiar and Maghous [3].

2.1 Homogenized viscoelastic properties in a medium with isotropic distribution of micro-fractures

To formulate non-aging viscoelastic properties of a homogenized medium involves the determination of the fourth-order relaxation tensor $\mathbb{R}^{\text{hom}}$ components since the boundary condition of the viscoelastic problem is an homogeneous strain $\underline{\underline{E}}$ applied to the fractured medium. In such conditions, the homogenized constitutive law for a fractured viscoelastic medium can be defined as:

$$\underline{\underline{\Sigma}} = \mathbb{R}^{\text{hom}} \circ \underline{\underline{E}} \qquad \textit{with} \qquad \mathbb{R}^{\text{hom}} = \left\langle \mathbb{C}^{s} \circ \mathbb{A} \right\rangle \tag{1}$$

where $\underline{\underline{\Sigma}}$ is the macroscopic stress, $\mathbb{A}$ is the strain concentration tensor associated with a representative elementary volume (REV) composed of a matrix and micro-fractures. The fourth-order matrix relaxation tensor is represented by $\mathbb{C}^{s}$, the symbol $\circ$ denotes the Boltzmann operator and the symbol $\langle\ \rangle$ represents the volume average over the matrix. In order to determine tensor $\mathbb{R}^{\text{hom}}$ is required to work with the elastic-viscoelastic correspondence principle. This principle enables to formulate the time-domain viscoelastic problem in terms of an equivalent elastic problem in the Laplace-Carson domain.

In view of all the above mentioned, it is possible to take advantage of the elastic properties of a fractured medium. It should be taken into account that in the elastic problem, fractures were considered as randomly oriented oblate ellipsoids. This particular feature can be considered as an isotropic distribution of fractures in the REV as shown in Fig. 1. It is also important to point out that for the determination of the homogenized stiffness tensor $\mathbb{C}^{\text{hom}}$ in the elastic problem, it was adopted the Mori-Tanaka linear homogenization scheme. The same scheme will be used for determination of the relaxation tensor in the Laplace-Carson space, which can be denoted by $\mathbb{R}^{\text{hom}*}$.

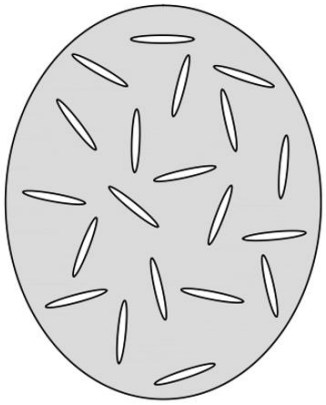

Figure 1. Isotropic distribution of fractures in the REV

After tensor $\mathbb{R}^{\text{hom}*}$ determination in Laplace-Carson domain, it becomes essential to express the relaxation tensor components in the real time domain. This raises the need for a specific inverse Laplace-Carson transform procedure $\mathbb{R}^{\text{hom}} = \mathcal{L}_c^{-1}\left(\mathbb{R}^{\text{hom}*}\right)$, which was developed by Aguiar and Maghous [3] in a simplified form. This procedure was conceived to work with the tensor $\mathbb{R}^{\text{hom}*}$ obtained from a Mori-Tanaka homogenization scheme when used classical rheological models for description of matrix and fractures behavior.

The relaxation function of a Generalized Maxwell rheological model in Fig. 2 has a mathematical equivalence with the results obtained by applying the inverse Laplace-Carson transform. From this equivalence, it can be stated that the mentioned rheological model represents the delayed behavior of non-aging linear viscoelastic materials and, therefore, it can be considered as the exact viscoelastic model.

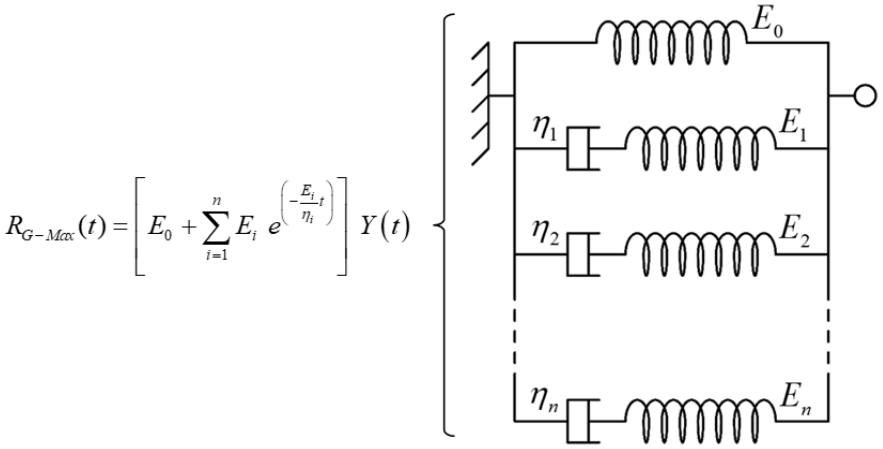

Figure 2. Generalized Maxwell model and its relaxation function

In the case of macroscopic isotropy, it is deduced that the bulk and shear viscoelastic behavior in Eq. (5) can also be exactly represented by a Generalized Maxwell rheological model, as displayed in Fig. 3.

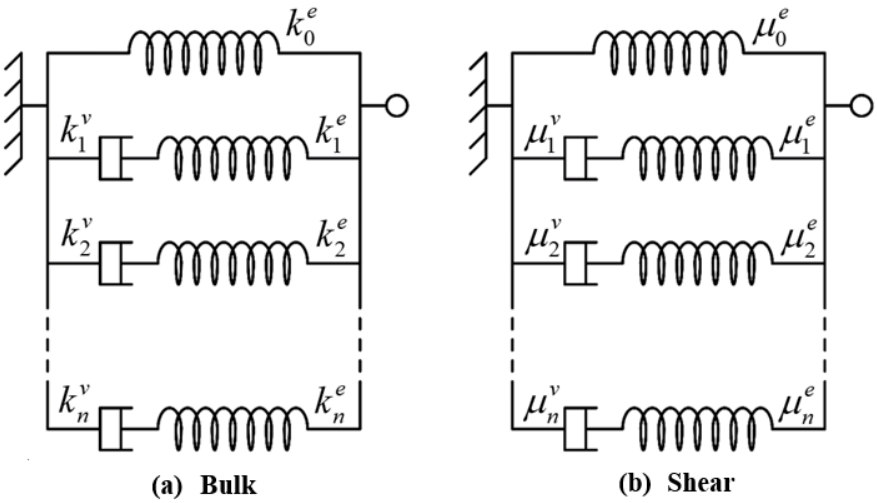

Figure 3. Generalized Maxwell model for viscoelastic moduli k^{hom} and μ^{hom}

In an isotropic distribution of randomly oriented fractures, tensor $\mathbb{R}^{\text{hom}}(t)$ depends on the viscoelastic moduli k^{hom} and μ^{hom}. In this way, taking advantage of the elastic-viscoelastic correspondence principle, viscoelastic moduli $k^{\text{hom}*}$ and $\mu^{\text{hom}*}$ in Laplace-Carson domain must be obtained in order to apply subsequently the inverse Laplace-Carson transform. The expressions for these viscoelastic moduli in Laplace-Carson domain are shown below:

$$k^{\text{hom}*} = \frac{k^{s*}}{1+\varepsilon\ \mathcal{M}_k} \quad ; \quad \mu^{\text{hom}*} = \frac{\mu^{s*}}{1+\varepsilon\ \mathcal{M}_\mu} \tag{2}$$

where $\varepsilon = \mathcal{N}a^3$ is the fracture density parameter, $\mathcal{N}$ is the number of fractures per unit volume and a is the radius of the oblate fracture. Aguiar and Maghous (2018) defined the dimensionless functions $\mathcal{M}_k\ (k^{s*}, \mu^{s*}, ak_n^*, ak_t^*)$ and $\mathcal{M}_\mu\ (k^{s*}, \mu^{s*}, ak_n^*, ak_t^*)$. Moduli $k^{\text{hom}*}$ and $\mu^{\text{hom}*}$ depend on the rheological models adopted by matrix and fractures. Now, only remains to apply the inverse Laplace-Carson transform procedure in order to obtain the moduli in time domain: $k^{\text{hom}}(t)$ and $\mu^{\text{hom}}(t)$.

3 Algorithm for time discretization of the viscoelastic model

It is necessary to develop a numerical programming scheme which considers a time discretization in the finite element framework. Essentially, what needs to be implemented is the viscoelastic constitutive law that describes the material behavior when applied a homogeneous strain boundary condition. Subroutines to be generated will be responsible for the calculation of homogenized stresses at Gauss points in finite element mesh of the analyzed structure. It is important that greek letters used for denote stress and strain macroscopic tensors will be $\underline{\underline{\Sigma}}$ and $\underline{\underline{E}}$, respectively.

The relaxation tensor can be expressed as $\mathbb{R}^{\text{hom}}(t) = 3\,k^{\text{hom}}(t)\,\mathbb{J} + 2\,\mu^{\text{hom}}(t)\,\mathbb{K}$ for an isotropic distribution of microfractures, where fourth-order tensors $\mathbb{J}$ and $\mathbb{K}$ are the spherical and deviatoric tensors, respectively. These tensors can be defined as $\mathbb{J} = \frac{1}{3}\underline{\underline{1}} \otimes \underline{\underline{1}}$ and $\mathbb{K} = \mathbb{I} - \mathbb{J}$, where $\mathbb{I}$ is the fourth-order unitary tensor. It must be emphasized that numerical expressions for the viscoelastic moduli are previously obtained by any calculus software.

Once the relaxation tensor $\mathbb{R}^{\text{hom}}(t)$ is computed, the macroscopic stress tensor can be determined, according to the constitutive law, as follows:

$$\underline{\underline{\Sigma}}(t) = \mathbb{R}^{\text{hom}}(t) : \underline{\underline{E}}(0) + \int_0^t \mathbb{R}^{\text{hom}}(s,t) : \frac{\partial \underline{\underline{E}}}{\partial s}(s)\, ds \tag{3}$$

where $\underline{\underline{E}}(0)$ is the instantaneous strain tensor that appear right in the moment of load application.

Regarding the code development, it will be considered n time steps with the same size Δt and $t_0 = 0$. For the $i+1$ time step, the corresponding time can be defined as:

$$t_{i+1} = t_i + \Delta t = (i+1)\cdot \Delta t \quad \textit{with} \quad i = 0, \ldots, n-1 \ . \tag{4}$$

An incremental procedure is applied in the integral equation in Eq. (3). Thus, the stress tensor at time t_{i+1}, is:

$$\underline{\underline{\Sigma}}(t_{i+1}) = \mathbb{R}^{\text{hom}}(t_{i+1}) : \underline{\underline{E}}(0) + \sum_{k=0}^{i} \left[\int_{t_k}^{t_{k+1}} \mathbb{R}^{\text{hom}}(s,t_{i+1}) : \frac{\partial \underline{\underline{E}}}{\partial s}(s)\, ds \right] . \tag{5}$$

A linear variation is assumed for the strain in the interval where the variable of integration $s \in \left[\, t_k, t_{k+1} \right]$. This assumption allows to express the derivative $\frac{\partial \underline{\underline{E}}}{\partial s}$ as:

$$\frac{\partial \underline{\underline{E}}}{\partial s} = \frac{\Delta \underline{\underline{E}}_{k+1}}{\Delta t} = \frac{\underline{\underline{E}}(t_{k+1}) - \underline{\underline{E}}(t_k)}{\Delta t} \ . \tag{6}$$

In order to update the stress tensor equation, Eq. (6) is replaced in Eq. (5). In a summarized form, the stress tensor $\underline{\underline{\Sigma}}(t_{i+1})$ can be expressed as:

$$\underline{\underline{\Sigma}}(t_{i+1}) = \underset{\sim}{K}^T : \Delta \underline{\underline{E}}_{i+1} + \underline{\underline{\Sigma}}^h(t) \tag{7}$$

where $\underset{\sim}{K}^T$ and $\underline{\underline{\Sigma}}^h(t)$ are fourth-order tensors defined as:

$$\begin{aligned} \underset{\sim}{K}^T &= \frac{1}{\Delta t}\left(\int_{t_i}^{t_{i+1}} \mathbb{R}^{\text{hom}}(s,t_{i+1})\, ds \right) \quad ; \quad \underline{\underline{\Sigma}}^h(t) = \underline{\underline{\Sigma}}^0(t_{i+1}) + \sum_{k=0}^{i-1} \left[\underset{\sim}{A}^{k+1} : \Delta \underline{\underline{E}}_{k+1} \right] \\ \underline{\underline{\Sigma}}^0(t_{i+1}) &= \mathbb{R}^{\text{hom}}(t_{i+1}) : \underline{\underline{E}}(0) \quad ; \quad \underset{\sim}{A}^{k+1} = \frac{1}{\Delta t}\left(\int_{t_k}^{t_{k+1}} \mathbb{R}^{\text{hom}}(s,t_{i+1})\, ds \right) \ . \end{aligned} \tag{8}$$

At this point, it must be remembered that the relaxation function for a Generalized Maxwell rheological model have mathematical equivalence with the relaxation tensor $\mathbb{R}^{\text{hom}}(t)$ components and it can be expressed in a generic way as:

$$R_{ijkl}(s,t) = R_{\infty} + \sum_{\alpha=1}^{p} R_{\alpha}\, e^{-\left(\frac{t-s}{\tau_{\alpha}}\right)} \qquad with \qquad \tau_{\alpha} = \frac{\eta_{\alpha}}{R_{\alpha}} \tag{9}$$

where R_{∞} stands for the stiffness of spring model. R_{α} and η_{α} are, respectively, the elastic spring stiffness and dashpot viscosity of branch α and p is the total number of branches. Since tensors $\underset{\sim}{K}^{T}$ and $\underset{\sim}{A}^{k+1}$ depend on tensor $\mathbb{R}^{\text{hom}}$, their components can be conveniently expressed as:

$$K_{ijkl}^{T} = R_{\infty} + \sum_{\alpha=1}^{p}\left[\frac{R_{\alpha}}{\left(\Delta t/\tau_{\alpha}\right)}\left(1-e^{-\left(\Delta t/\tau_{\alpha}\right)}\right)\right]\ ;\ A_{ijkl}^{k+1} = R_{\infty} + \sum_{\alpha=1}^{p}\left[\frac{R_{\alpha}}{\left(\Delta t/\tau_{\alpha}\right)}\left(e^{-(i-k)\left(\frac{\Delta t}{\tau_{\alpha}}\right)} - e^{-(i-k+1)\left(\frac{\Delta t}{\tau_{\alpha}}\right)}\right)\right]. \tag{10}$$

It is known that in an isotropic distribution of fractures, for the non-zero components of tensor $\mathbb{R}^{\text{hom}}$, the following applies:

$$R_{1111}^{\text{hom}} = R_{2222}^{\text{hom}} = R_{3333}^{\text{hom}}\ ;\ R_{1212}^{\text{hom}} = R_{1313}^{\text{hom}} = R_{2323}^{\text{hom}}\ ;\ R_{1122}^{\text{hom}} = R_{1133}^{\text{hom}} = R_{2211}^{\text{hom}} = R_{2233}^{\text{hom}} = R_{3311}^{\text{hom}} = R_{3322}^{\text{hom}}\ . \tag{11}$$

The same equalities shown in Eq. (11) applies also to tensors $\underset{\sim}{K}^{T}$ and $\underset{\sim}{A}^{k+1}$. Now, considering Eq. (5), it can be determined the expressions for non-zero components of tensor $\underset{\sim}{K}^{T}$:

$$K_{1111}^{T} = \frac{a_0^{\omega}}{b_0^{\omega}} + \sum_{\alpha=1}^{n\omega}\left(\frac{D_{\alpha}^{\omega}}{\left(-R_{\alpha}^{\omega}\,\Delta t\right)}\left(1-e^{R_{\alpha}^{\omega}\,\Delta t}\right)\right) + \frac{4}{3}\left[\frac{a_0^{\mu}}{b_0^{\mu}} + \sum_{\alpha=1}^{n\mu}\left(\frac{D_{\alpha}^{\mu}}{\left(-R_{\alpha}^{\mu}\,\Delta t\right)}\left(1-e^{R_{\alpha}^{\mu}\,\Delta t}\right)\right)\right] \tag{12}$$

$$K_{1122}^{T} = \frac{a_0^{\omega}}{b_0^{\omega}} + \sum_{\alpha=1}^{n\omega}\left(\frac{D_{\alpha}^{\omega}}{\left(-R_{\alpha}^{\omega}\,\Delta t\right)}\left(1-e^{R_{\alpha}^{\omega}\,\Delta t}\right)\right) - \frac{2}{3}\left[\frac{a_0^{\mu}}{b_0^{\mu}} + \sum_{\alpha=1}^{n\mu}\left(\frac{D_{\alpha}^{\mu}}{\left(-R_{\alpha}^{\mu}\,\Delta t\right)}\left(1-e^{R_{\alpha}^{\mu}\,\Delta t}\right)\right)\right] \tag{13}$$

$$K_{1212}^{T} = 2\left[\frac{a_0^{\mu}}{b_0^{\mu}} + \sum_{\alpha=1}^{n\mu}\left(\frac{D_{\alpha}^{\mu}}{\left(-R_{\alpha}^{\mu}\,\Delta t\right)}\left(1-e^{R_{\alpha}^{\mu}\,\Delta t}\right)\right)\right] \tag{14}$$

Similarly, for tensor $\underset{\sim}{A}^{k+1}$, the corresponding non-zero components are:

$$A_{1111}^{k+1} = \frac{a_0^{\omega}}{b_0^{\omega}} + \sum_{\alpha=1}^{n\omega}\left(\frac{D_{\alpha}^{\omega}\left(e^{(i-k)\,R_{\alpha}^{\omega}\,\Delta t} - e^{(i-k+1)\,R_{\alpha}^{\omega}\,\Delta t}\right)}{\left(-R_{\alpha}^{\omega}\,\Delta t\right)}\right) + \frac{4}{3}\left[\frac{a_0^{\mu}}{b_0^{\mu}} + \sum_{\alpha=1}^{n\mu}\left(\frac{D_{\alpha}^{\mu}\left(e^{(i-k)\,R_{\alpha}^{\mu}\,\Delta t} - e^{(i-k+1)\,R_{\alpha}^{\mu}\,\Delta t}\right)}{\left(-R_{\alpha}^{\mu}\,\Delta t\right)}\right)\right] \tag{15}$$

$$A_{1122}^{k+1} = \frac{a_0^{\omega}}{b_0^{\omega}} + \sum_{\alpha=1}^{n\omega}\left(\frac{D_{\alpha}^{\omega}\left(e^{(i-k)\,R_{\alpha}^{\omega}\,\Delta t} - e^{(i-k+1)\,R_{\alpha}^{\omega}\,\Delta t}\right)}{\left(-R_{\alpha}^{\omega}\,\Delta t\right)}\right) - \frac{2}{3}\left[\frac{a_0^{\mu}}{b_0^{\mu}} + \sum_{\alpha=1}^{n\mu}\left(\frac{D_{\alpha}^{\mu}\left(e^{(i-k)\,R_{\alpha}^{\mu}\,\Delta t} - e^{(i-k+1)\,R_{\alpha}^{\mu}\,\Delta t}\right)}{\left(-R_{\alpha}^{\mu}\,\Delta t\right)}\right)\right] \tag{16}$$

$$A_{1212}^{k+1} = 2\left[\frac{a_0^{\mu}}{b_0^{\mu}} + \sum_{\alpha=1}^{n\mu}\left(\frac{D_{\alpha}^{\mu}\left(e^{(i-k)\,R_{\alpha}^{\mu}\,\Delta t} - e^{(i-k+1)\,R_{\alpha}^{\mu}\,\Delta t}\right)}{\left(-R_{\alpha}^{\mu}\,\Delta t\right)}\right)\right] \tag{17}$$

where ω corresponds to the bulk relaxation modulus and μ to the shear relaxation modulus.

The precedent equations make possible the stress calculation at Gauss point for all the considered step times. According to the way the stress tensor was formulated in Eq. (7), it is proposed to define the stress tensor components for three different time steps: TS = 1, TS = 2 and TS ≥ 3.

For TS = 1, where $t_{i+1} = t_1$ and $i = 0$, the stress tensor $\underline{\underline{\sigma}}^{TS}$ can be defined as:

$$\underline{\underline{\sigma}}^{1} = \underset{\sim}{K}^{T} : \Delta\underline{\underline{\varepsilon}}^{1} \; + \; \mathbb{R}^{1} : \underline{\underline{\varepsilon}}^{0} \tag{18}$$

$$\begin{bmatrix} \sigma_{11}^{1} \\ \sigma_{22}^{1} \\ \sigma_{33}^{1} \\ \sigma_{12}^{1} \\ \sigma_{13}^{1} \\ \sigma_{23}^{1} \end{bmatrix} = \begin{bmatrix} K_{1111}^{T}\,\Delta\varepsilon_{11}^{1} + K_{1122}^{T}\,\Delta\varepsilon_{22}^{1} + R_{1111}^{1}\,\varepsilon_{11}^{0} + R_{1122}^{1}\,\varepsilon_{22}^{0} \\ K_{1111}^{T}\,\Delta\varepsilon_{22}^{1} + K_{1122}^{T}\,\Delta\varepsilon_{11}^{1} + R_{1111}^{1}\,\varepsilon_{22}^{0} + R_{1122}^{1}\,\varepsilon_{11}^{0} \\ K_{1122}^{T}\,\Delta\varepsilon_{11}^{1} + K_{1122}^{T}\,\Delta\varepsilon_{22}^{1} + R_{1122}^{1}\,\varepsilon_{11}^{0} + R_{1122}^{1}\,\varepsilon_{22}^{0} \\ K_{1212}^{T}\,\Delta\varepsilon_{12}^{1} + R_{1212}^{1}\,\varepsilon_{12}^{0} \\ 0 \\ 0 \end{bmatrix}. \tag{19}$$

For TS = 2, where $t_{i+1} = t_2$ and $i = 1$, the stress tensor $\underline{\underline{\sigma}}^{TS}$ can be defined as:

$$\underline{\underline{\sigma}}^{2} = \underset{\sim}{K}^{T} : \Delta\underline{\underline{\varepsilon}}^{2} \; + \; \mathbb{R}^{2} : \underline{\underline{\varepsilon}}^{0} + \underset{\sim}{A}^{1} : \Delta\underline{\underline{\varepsilon}}^{1} \tag{20}$$

$$\begin{bmatrix} \sigma_{11}^{2} \\ \sigma_{22}^{2} \\ \sigma_{33}^{2} \\ \sigma_{12}^{2} \\ \sigma_{13}^{2} \\ \sigma_{23}^{2} \end{bmatrix} = \begin{bmatrix} K_{1111}^{T}\,\Delta\varepsilon_{11}^{2} + K_{1122}^{T}\,\Delta\varepsilon_{22}^{2} + R_{1111}^{2}\,\varepsilon_{11}^{0} + R_{1122}^{2}\,\varepsilon_{22}^{0} + A_{1111}^{1}\,\Delta\varepsilon_{11}^{1} + A_{1122}^{1}\,\Delta\varepsilon_{22}^{1} \\ K_{1111}^{T}\,\Delta\varepsilon_{22}^{2} + K_{1122}^{T}\,\Delta\varepsilon_{11}^{2} + R_{1111}^{2}\,\varepsilon_{22}^{0} + R_{1122}^{2}\,\varepsilon_{11}^{0} + A_{1111}^{1}\,\Delta\varepsilon_{22}^{1} + A_{1122}^{1}\,\Delta\varepsilon_{11}^{1} \\ K_{1122}^{T}\,\Delta\varepsilon_{11}^{2} + K_{1122}^{T}\,\Delta\varepsilon_{22}^{2} + R_{1122}^{2}\,\varepsilon_{11}^{0} + R_{1122}^{2}\,\varepsilon_{22}^{0} + A_{1122}^{1}\,\Delta\varepsilon_{11}^{1} + A_{1122}^{1}\,\Delta\varepsilon_{22}^{1} \\ K_{1212}^{T}\,\Delta\varepsilon_{12}^{2} + R_{1212}^{2}\,\varepsilon_{12}^{0} + A_{1212}^{1}\,\Delta\varepsilon_{12}^{1} \\ 0 \\ 0 \end{bmatrix}. \tag{21}$$

For TS ≥ 3, where $t_{i+1} \geq t_3$, $i = TS - 1$ and $k \in [0, i-1]$, the stress tensor $\underline{\underline{\sigma}}^{TS}$ can be defined as:

$$\underline{\underline{\sigma}}^{TS} = \underset{\sim}{K}^{T} : \Delta\underline{\underline{\varepsilon}}^{TS} \; + \; \mathbb{R}^{TS} : \underline{\underline{\varepsilon}}^{0} + \sum_{k=0}^{i-1} \left[\underset{\sim}{A}^{k+1} : \Delta\underline{\underline{\varepsilon}}^{k+1} \right]. \tag{22}$$

The matrix form of tensor $\underline{\underline{\sigma}}^{TS}$ for TS ≥ 3 is presented below:

$$\begin{bmatrix} \sigma_{11}^{\mathrm{NTR}} \\ \sigma_{22}^{\mathrm{NTR}} \\ \sigma_{33}^{\mathrm{NTR}} \\ \sigma_{12}^{\mathrm{NTR}} \\ \sigma_{13}^{\mathrm{NTR}} \\ \sigma_{23}^{\mathrm{NTR}} \end{bmatrix} = \begin{bmatrix} K_{1111}^{T}\,\Delta\varepsilon_{11}^{NTR} + K_{1122}^{T}\,\Delta\varepsilon_{22}^{NTR} + R_{1111}^{NTR}\,\varepsilon_{11}^{0} + R_{1122}^{NTR}\,\varepsilon_{22}^{0} + \mathrm{SAE11} \\ K_{1111}^{T}\,\Delta\varepsilon_{22}^{NTR} + K_{1122}^{T}\,\Delta\varepsilon_{11}^{NTR} + R_{1111}^{NTR}\,\varepsilon_{22}^{0} + R_{1122}^{NTR}\,\varepsilon_{11}^{0} + \mathrm{SAE22} \\ K_{1122}^{T}\,\Delta\varepsilon_{11}^{NTR} + K_{1122}^{T}\,\Delta\varepsilon_{22}^{NTR} + R_{1122}^{NTR}\,\varepsilon_{11}^{0} + R_{1122}^{NTR}\,\varepsilon_{22}^{0} + \mathrm{SAE33} \\ K_{1212}^{T}\,\Delta\varepsilon_{12}^{NTR} + R_{1212}^{NTR}\,\varepsilon_{12}^{0} + \mathrm{SAE12} \\ 0 \\ 0 \end{bmatrix} \tag{23}$$

where SAE11, SAE22, SAE33 and SAE12 are defined as:

$$\text{SAE11} = \sum_{k=0}^{i-1} \left(A_{1111}^{k+1} \, \Delta\varepsilon_{11}^{k+1} + A_{1122}^{k+1} \, \Delta\varepsilon_{22}^{k+1} \right)$$

$$\text{SAE22} = \sum_{k=0}^{i-1} \left(A_{1111}^{k+1} \, \Delta\varepsilon_{22}^{k+1} + A_{1122}^{k+1} \, \Delta\varepsilon_{11}^{k+1} \right) \tag{24}$$

$$\text{SAE33} = \sum_{k=0}^{i-1} \left(A_{1122}^{k+1} \, \Delta\varepsilon_{11}^{k+1} + A_{1122}^{k+1} \, \Delta\varepsilon_{22}^{k+1} \right) \quad ; \quad \text{SAE12} = \sum_{k=0}^{i-1} \left(A_{1212}^{k+1} \, \Delta\varepsilon_{12}^{k+1} \right).$$

From Eq. (24), $\Delta\underline{\underline{\varepsilon}}^1 = \underline{\underline{\varepsilon}}^1 - \underline{\underline{\varepsilon}}^0$ and $\mathbb{R}^1$ is the homogenized relaxation tensor evaluated at TS=1. It is known that $\underline{\underline{\varepsilon}}^0$ is the instantaneous strain tensor. The matrix form of tensor $\underline{\underline{\sigma}}^1$ is found in Eq. (19). From Eq. (26), $\Delta\underline{\underline{\varepsilon}}^2 = \underline{\underline{\varepsilon}}^2 - \underline{\underline{\varepsilon}}^1$ and $\mathbb{R}^2$ is the homogenized relaxation tensor evaluated at TS=2. $\underset{\sim}{A}^1$ is the tensor $\underset{\sim}{A}^{k+1}$ evaluated at TS=1 ($k = 0$). The matrix form of tensor $\underline{\underline{\sigma}}^2$ is found in Eq. (21).

Finally, Eq. (19), (21) and (23) can be considered as the basis for the implementation code.

4 Verification of the implementation code

This section is focused on the verification of the implementation code through the analysis of three examples of application under plane strain conditions. Each one of them presents a time-dependent analytical solution that will be compared with the corresponding numerical responses. The correspondence between the delayed responses will serve to verify the developed code.

It will be used the same specimen for the three examples. With respect to the specimen dimensions, it is a quadrilateral with a height and base of 1.00 m. Concerning the discretized geometric model, it is composed of four quadrilateral finite elements, even though it is possible to use just one finite element since stress and strain fields are homogeneous for all these examples. Fig. 4 displays the finite elements, nodes and dimensions of the geometric model.

With regard to viscoelastic characteristics of the material, the related parameters depend on the rheological model chosen to describe matrix and fractures behavior. The general case considers a Burger rheological model for representation of the matrix and fractures delayed behavior. However, for the examples in this paper, it will be analyzed a particular case of viscoelastic behavior that combine rheological models adopted by the material constituents. In this case, matrix adopt a Burger rheological model and fractures adopt a Maxwell rheological model.

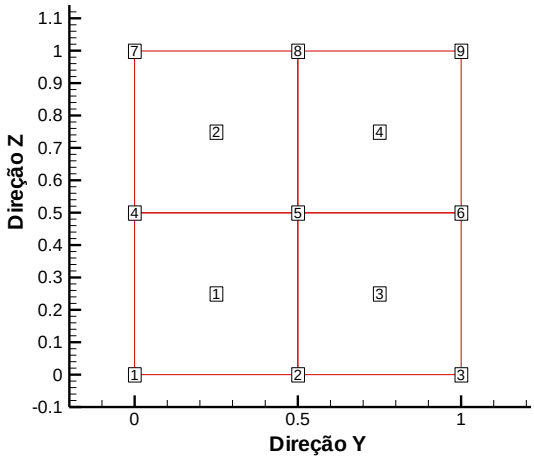

Figure 4. Elements of the discretized geometric model

Figure 5 displays the rheological model elements and their corresponding parameters for case

Burger-Maxwell case. Tables 1 and 2 show, respectively, the mechanical parameters used for matrix and fractures. The fracture density parameter is $\varepsilon = 0.20$ and the number of fractures per unit volume $\mathcal{N} = 1.0$.

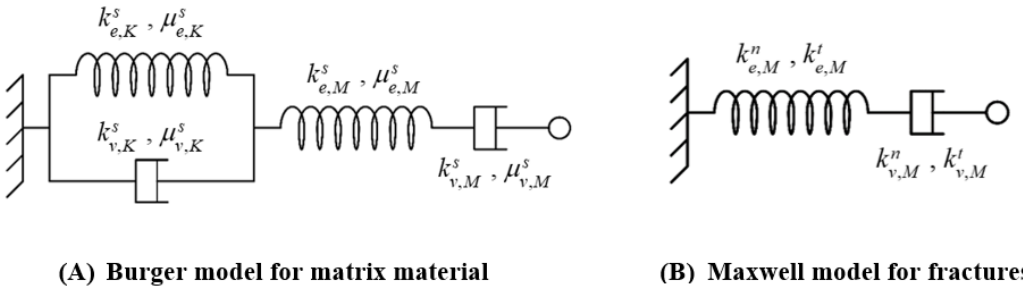

Figure 5. Rheological model elements for Burger-Maxwell case

Burger model is composed by a Maxwell component (subscript M) connected in series with a Kelvin component (subscript K). With respect to matrix material, elastic parameters associated with a spring in bulk are denoted by $k^s_{e,M}$ and $k^s_{e,K}$, whereas that associated in shear are $\mu^s_{e,M}$ and $\mu^s_{e,K}$. Viscosity parameters associated to a dashpot in bulk are denoted by $k^s_{v,M}$ and $k^s_{v,K}$, whereas that associated in shear are $\mu^s_{v,M}$ and $\mu^s_{v,K}$.

Table 1. Matrix mechanical parameters for Burger model

MATRIX					
Parameter	**Value**	**Unit**	**Parameter**	**Value**	**Unit**
$k^s_{e,M}$	24.42	GPa	$k^s_{e,K}$	39.27	GPa
$k^s_{v,M}$	7.33×10^8	GPa-s	$k^s_{v,K}$	5.07×10^7	GPa-s
$\mu^s_{e,M}$	13.27	GPa	$\mu^s_{e,K}$	14.07	GPa
$\mu^s_{v,M}$	3.88×10^8	GPa-s	$\mu^s_{v,K}$	1.27×10^7	GPa-s

As regards the fractures behavior, the elastic parameter associated with a spring under normal stress is denoted by $k^n_{e,M}$, whereas that associated under tangential stress is $k^t_{e,M}$. The viscosity parameter associated to a dashpot under normal stress is denoted by $k^n_{v,M}$, whereas that associated under tangential stress is $k^t_{v,M}$.

Table 2. Fractures mechanical parameters for Maxwell model

FRACTURES		
Parameter	**Value**	**Unit**
$k^n_{e,M}$	42.22	GPa / m
$k^n_{v,M}$	7x107	GPa-s / m
$k^t_{e,M}$	16.88	GPa / m
$k^t_{v,M}$	4x107	GPa-s / m

4.1 Example 1: Compression under prescribed stress

Figure 6 shows a specimen with height H subjected to constant compressive stress $-\sigma \cdot Y(t)$ under plane strain conditions, where $Y(t)$ denotes the Heaviside step function at origin. Material will be considered homogeneous, isotropic and linear viscoelastic. The initial stress state is $\underline{\underline{\sigma}}^0 = 0$.

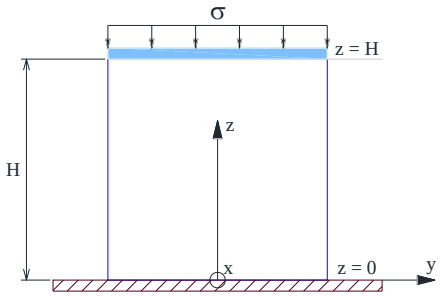

Figure 6. YZ-plane for specimen subjected to compressive stress

The problem solution involves the calculation of time-dependent stress and displacement fields $\left(\underline{\underline{\sigma}}(t), \underline{\xi}(\underline{X}, t)\right)$ by using basic concepts of continuum mechanics [6] and viscoelasticity [7]. The analytical solution tensorial fields are:

$$\underline{\xi}\,(\underline{X}, t) = \left[\frac{-\sigma\ \left(2\,\mu'(t) - 3\,k'(t)\right)}{4\,\mu'(t)\left(3\,k'(t) + \mu'(t)\right)}\right] y\ \underline{e}_y + \left[\frac{-\sigma\ \left(3\,k'(t) + 4\,\mu'(t)\right)}{4\,\mu'(t)\left(3\,k'(t) + \mu'(t)\right)}\right] z\ \underline{e}_z$$

$$\underline{\underline{\sigma}}(t) = \left[\frac{-\sigma\ \left(3\,k'(t) - 2\,\mu'(t)\right)}{2\ \left(3\,k'(t) + \mu'(t)\right)}\right] \underline{e}_x \otimes \underline{e}_x - \sigma\ \underline{e}_z \otimes \underline{e}_z \tag{25}$$

where $k'(t)$ stands for viscoelastic bulk modulus and $\mu'(t)$ for viscoelastic shear modulus. Variables y and z compose position vector $\underline{X}$. These moduli are defined as:

$$k'(t) = \frac{1}{\mathcal{L}_c^{-1}\left(1/\,k_{(p)}^{\text{hom}*}\right)} \quad ; \quad \mu'(t) = \frac{1}{\mathcal{L}_c^{-1}\left(1/\,\mu_{(p)}^{\text{hom}*}\right)} \tag{26}$$

where $k_{(p)}^{\text{hom}*}$ and $\mu_{(p)}^{\text{hom}*}$ are the homogenized bulk and shear moduli in Laplace-Carson domain, respectively. It will be considered a compressive stress $\sigma = 0.02\ GPa$ for calculations. In relation to Burger-Maxwell case, below is shown the comparison between analytical solution defined in Eq. (25) and numerical response for vertical strain ε_{zz} and horizontal strain ε_{yy}.

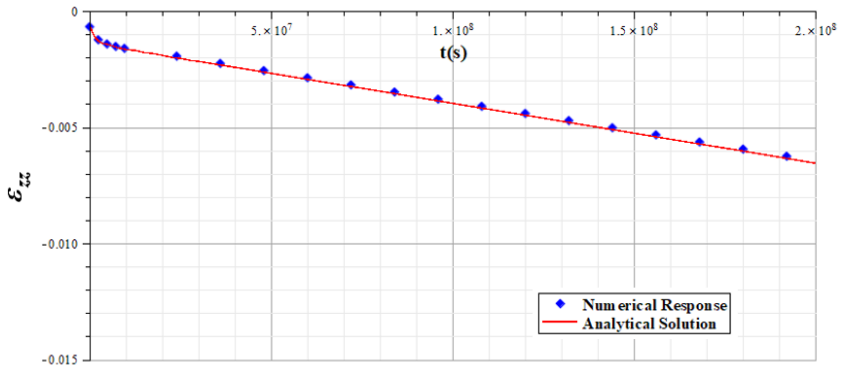

Figure 7. Comparison of delayed responses for vertical strain ε_{zz} (Burger-Maxwell)

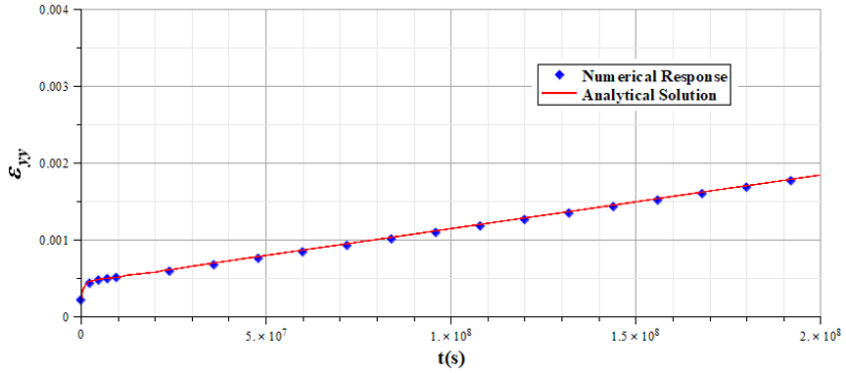

Figure 8. Comparison of delayed responses for horizontal strain ε_{yy} (Burger-Maxwell)

As shown in Fig. 7-8, analytical and numerical curves present a satisfactory correspondence. Consequently, the implementation code has been successfully verified.

4.2 Example 2: Compression under prescribed displacement

Figure 9 shows a specimen with height H subjected to a vertical imposed displacement $-\delta_z\ Y(t)\ \underline{e}_z$ under plane strain conditions. Material will be considered homogeneous, isotropic and linear viscoelastic. The initial stress state is $\underline{\underline{\sigma}}^0 = 0$.

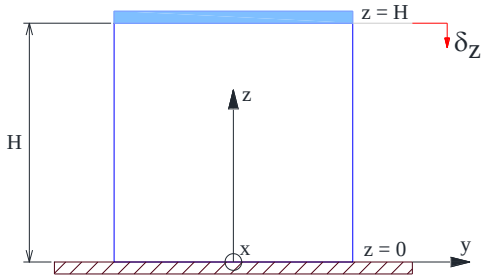

Figure 9. YZ-plane for specimen subjected to constant vertical displacement

As seen in section 4.1, the problem solution involves the calculation of time-dependent stress and displacement fields $\left(\underline{\underline{\sigma}}(t), \underline{\xi}(\underline{X}, t)\right)$. The analytical solution tensorial fields are:

$$\underline{\xi}(\underline{X},t) = \left[-\left(\frac{3\,k(t) - 2\,\mu(t)}{3\,k(t) + 4\,\mu(t)} \right) \varepsilon_z\ y \right] \underline{e}_y + \varepsilon_z\ z\ \underline{e}_z$$

$$\underline{\underline{\sigma}}(t) = \left[\frac{2\,\mu(t)\ \left(3\,k(t) - 2\,\mu(t)\right)}{\left(3\,k(t) + 4\,\mu(t)\right)}\ \varepsilon_z \right] \underline{e}_x \otimes \underline{e}_x + \left[\frac{4\,\mu(t)\left(3\,k(t) + \mu(t)\right)}{\left(3\,k(t) + 4\,\mu(t)\right)}\ \varepsilon_z \right] \underline{e}_z \otimes \underline{e}_z \tag{27}$$

where variables y and z compose position vector $\underline{X}$. The strain caused by imposed displacement is denoted by $\varepsilon_z = -\delta_z / H$. The bulk and shear moduli in time domain are denoted by $k(t)$ and $\mu(t)$, respectively. The numerical expressions of $k(t)$ and $\mu(t)$ can be obtained by means of some calculus software and depend on the rheological models adopted for matrix and fractures.

It will be considered an imposed displacement $\delta_z = 0.01\,\text{m}.$ for calculations. In relation to Burger-Maxwell case, below is shown the comparison between analytical solution defined in Eq. (27) and numerical response for vertical stress σ_{zz} and stress σ_{xx} perpendicular to YZ-plane.

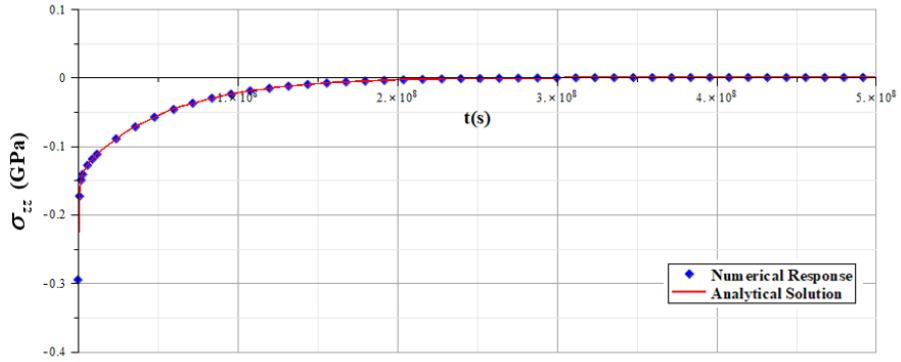

Figure 10. Comparison of delayed responses for stress σ_{zz} (Burger-Maxwell)

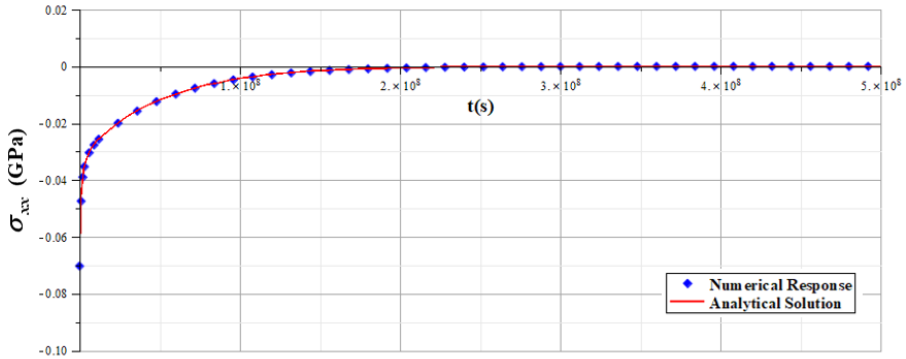

Figure 11. Comparison of delayed responses for stress σ_{xx} (Burger-Maxwell)

As shown in Fig. 10-11, analytical and numerical curves present a satisfactory correspondence. Consequently, the implementation code has been successfully verified.

4.3 Example 3: Compression under prescribed displacement rate

Figure 12 shows a specimen with height H subjected to a constant imposed displacement rate $\dot{\delta}_z$ under plane strain conditions. The applied displacement is defined as $-\delta_z(t) = -\left(\dot{\delta}_z\ t + \delta_{z0}\right)\ Y(t)$, where δ_{z0} stands for the vertical displacement imposed at the time $t = 0^+$.

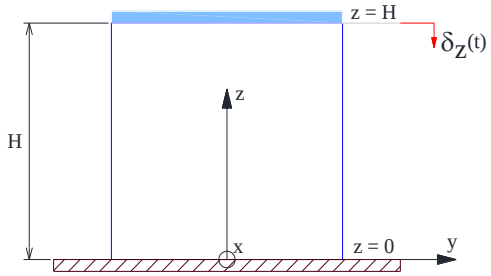

Figure 12. YZ-plane for specimen subjected to constant vertical displacement rate

Material will be considered homogeneous, isotropic and linear viscoelastic. The initial stress state will be considered as $\underline{\underline{\sigma}}^0 = 0$ and the strain $\varepsilon_z(t)$ related to displacement $-\delta_z(t)$ can be expressed as:

$$\varepsilon_z(t) = -\left(\dot{\delta}_z / H\ \ t + \delta_{z0}/H\right)\ Y(t) = -\left(\dot{\varepsilon}_z\ t + \varepsilon_{z0}\right)\ Y(t) \tag{28}$$

where $\dot{\varepsilon}_z$ can be considered as the vertical strain rate and ε_{z0} as the instantaneous vertical strain. The analytical solution tensorial fields are:

$$\underline{\xi}(\underline{X},t)=\left[\left(\dot{\varepsilon}_y\ t+\varepsilon_{y0}\right)\ y\right]\ \underline{e}_y+\left[\left(\dot{\varepsilon}_z\ t+\varepsilon_{z0}\right)\ z\right]\ \underline{e}_z$$

$$\begin{aligned}\underline{\underline{\sigma}}(t)=&\left[\left(\dot{\varepsilon}_y+\dot{\varepsilon}_z\right)\ \left(\int_0^t R_{1122}^{(s,t)}\ ds\right)+\left(\varepsilon_{y0}+\varepsilon_{z0}\right)\ \left(R_{1122}^{(t)}\right)\right]\ \underline{e}_x\otimes\underline{e}_x+\\&\left[\dot{\varepsilon}_y\ \left(\int_0^t R_{1111}^{(s,t)}\ ds\right)+\dot{\varepsilon}_z\ \left(\int_0^t R_{1122}^{(s,t)}\ ds\right)+\varepsilon_{y0}\ R_{1111}^{(t)}+\varepsilon_{z0}\ R_{1122}^{(t)}\right]\ \underline{e}_y\otimes\underline{e}_y+\\&\left[\dot{\varepsilon}_y\ \left(\int_0^t R_{1122}^{(s,t)}\ ds\right)+\dot{\varepsilon}_z\ \left(\int_0^t R_{1111}^{(s,t)}\ ds\right)+\varepsilon_{y0}\ R_{1122}^{(t)}+\varepsilon_{z0}\ R_{1111}^{(t)}\right]\ \underline{e}_z\otimes\underline{e}_z\end{aligned}\tag{29}$$

where $R_{1111}^{(s,t)}$ and $R_{1122}^{(s,t)}$ are relaxation tensor $\mathbb{R}(t)$ components. The instantaneous horizontal strain ε_{y0} can be obtained from the viscoelastic solution shown in section 4.2. Horizontal strain rate $\dot{\varepsilon}_y$ is:

$$\dot{\varepsilon}_y=\frac{-\dot{\varepsilon}_z\ \left(\int_0^t R_{1122}^{(s,t)}\ ds\right)-\varepsilon_{y0}\ R_{1111}^{(t)}-\varepsilon_{z0}\ R_{1122}^{(t)}}{\left(\int_0^t R_{1111}^{(s,t)}\ ds\right)}\ .\tag{30}$$

It will be considered an imposed instantaneous displacement $\delta_{z0}=0.001\,\text{m}.$ and a displacement rate $\dot{\delta}_z=10^{-8}\ m/s$ for calculations. In relation to Burger-Maxwell case, below is shown the comparison between analytical solution defined in Eq. (29) and numerical response for vertical stress σ_{zz} and stress σ_{xx} perpendicular to YZ-plane.

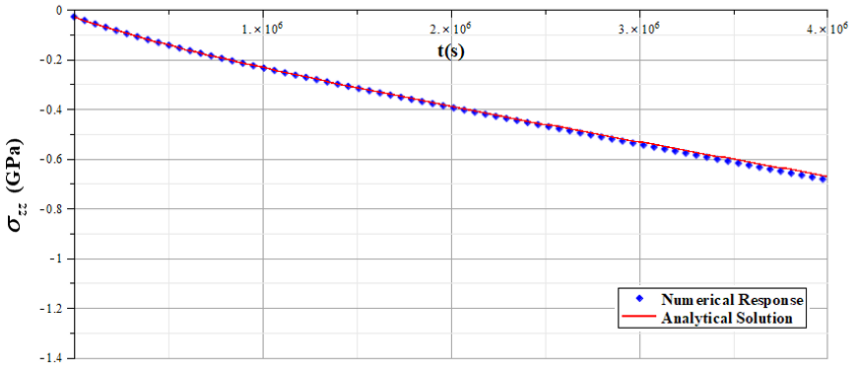

Figure 13. Comparison of delayed responses for stress σ_{zz} (Burger-Maxwell)

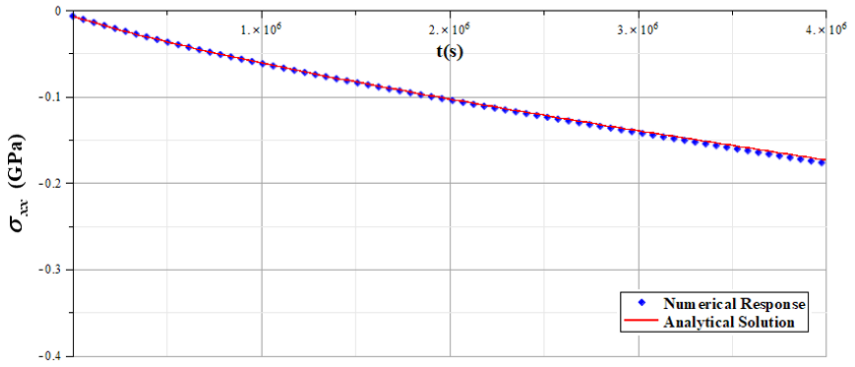

Figure 14. Comparison of delayed responses for stress σ_{xx} (Burger-Maxwell)

As shown in Fig. 13-14, analytical and numerical curves present an acceptable correspondence. Consequently, the implementation code has been successfully verified for all the examples presented in this section.

5 Analysis of delayed behavior of deep underground galleries

In addition to verification showed in section 4, the present section is focused on the analysis of geo-structures of greater complexity under plane strain conditions. There exist some geo-structures that allows this type of analysis, such as the deep underground galleries or tunnels that enables to determine a cross-section of interest for carrying out a bidimensional analysis. It will be considered two types of cross-section for deep tunnels: circular and horseshoe. Concerning to circular cross-section, there will be presented two situations: unlined cross-section and lined cross-section. Subsequently, for a horseshoe cross-section, it will be analyzed its delayed response in order to highlight the predictive capabilities of this computational tool when it is not possible to have an analytical solution for viscoelastic behavior.

5.1 Unlined circular cross-section tunnel

The hypotheses considered in this problem are mentioned as follows. The tunnel has radius R and a depth H, where $\mathrm{H} \gg \mathrm{R}$. The massif material is homogeneous and isotropic. The excavation process will be regarded as instantaneous. The initial stress (geostatic) $\underline{\underline{\sigma}}^0 = -p\,\underline{\underline{1}}$, due to self-weight of the massif, will be uniform in the region around the gallery. The variable p is defined as $p = \gamma H$, where γ represents the specific weight of the massif. Height and base will be L, where $L < H$ (Fig. 15).

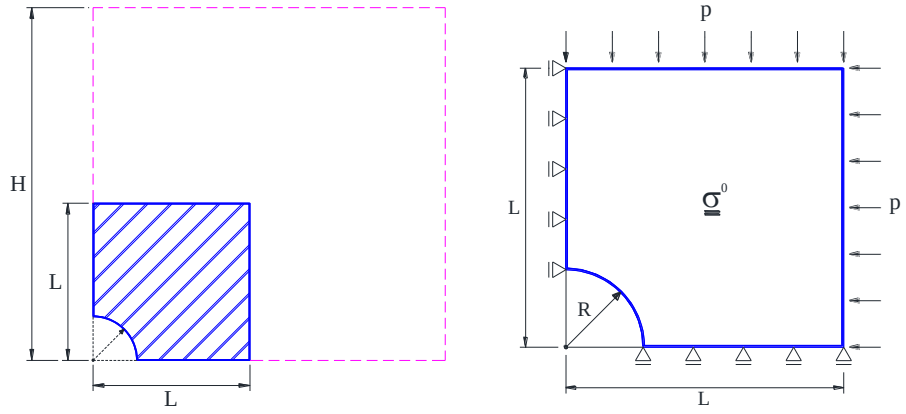

Figure 15. Dimensions and boundary conditions for the geometric model

The analytical solution involving delayed response will be shown in polar coordinates. According to Bernaud [8], position vector $\underline{X} = r \cdot \underline{e}_r$ does not depend on the angular coordinate, where r is the radial distance. Instant after excavation is t_0^+. The solution fields are shown as follows:

$$\underline{\xi}(r,t) = -\frac{pR^2}{r} M(t,t_0^+)\ \underline{e}_r$$

$$\underline{\underline{\sigma}}(r,t) = \left[p\left(\frac{R^2}{r^2} Y_{t_0^+}(t) - 1 \right) \right] \underline{e}_r \otimes \underline{e}_r + \left[-p\left(\frac{R^2}{r^2} Y_{t_0^+}(t) + 1 \right) \right] \underline{e}_\theta \otimes \underline{e}_\theta + (-p)\,\underline{e}_z \otimes \underline{e}_z \tag{31}$$

where $Y_{t_0^+}(t)$ is the Heaviside function for $t > t_0^+$ and the modulus $M(t,t_0^+)$ depends on the rheological models adopted by the matrix and fractures. This modulus can be defined as:

$$M(t,t_0^+) = \mathcal{L}_c^{-1}\left(\frac{1}{2\mu^*(p)}\right) \tag{32}$$

where $\mu^*(p)$ is the shear relaxation modulus in Laplace-Carson domain. The radial convergence is an important parameter related to the displacements in unlined cross-sections and can be expressed as:

$$U(t) = -\frac{\xi(R,t)}{R} = pM(t,t_0^+)\,. \tag{33}$$

It will be considered a depth $\mathrm{H} = 125.00$ m., radius $\mathrm{R} = 2.50$ m., specific weight $\gamma = 24000\ N/m^3$ for calculations. The lateral and vertical pressure exerted by massif is $p = 0.003$ GPa. Concerning to viscoelastic characteristics of the material, the case of delayed behavior adopted by matrix and fractures is Burger-Maxwell. Consequently, mechanical parameters correspond to those specified in Tables 1 and 2, as well as the fracture density parameter ε and the number of fractures per unit volume $\mathcal{N}$. Regarding to the discretized geometric model, Fig. 16 shows the finite element mesh used for the analyses. It is composed of 192 finite element and 221 nodes.

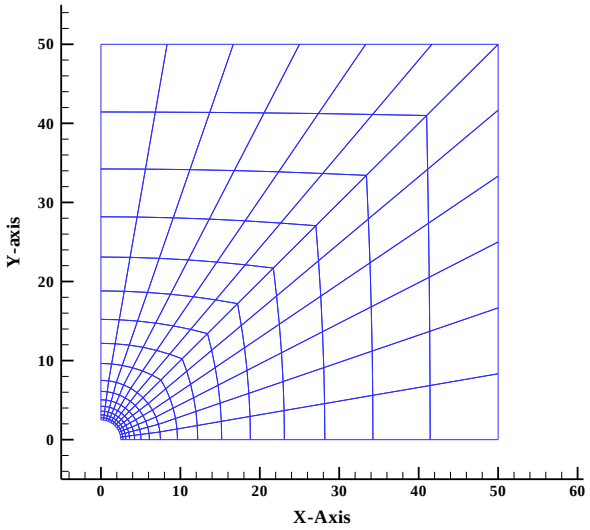

Figure 16. Finite element mesh for circular cross-section tunnel

In relation to Burger-Maxwell case, the analytical solution, defined in Eq. (31), will be compared with the numerical response for radial displacement $\xi_{rr}(r,t)$ and radial stress $\sigma_{rr}(r,t)$. The analysis will be performed for three different times: *t1* corresponds to the instantaneous elastic response, *t2* is an intermediate time and *t3* corresponds to a very long time.

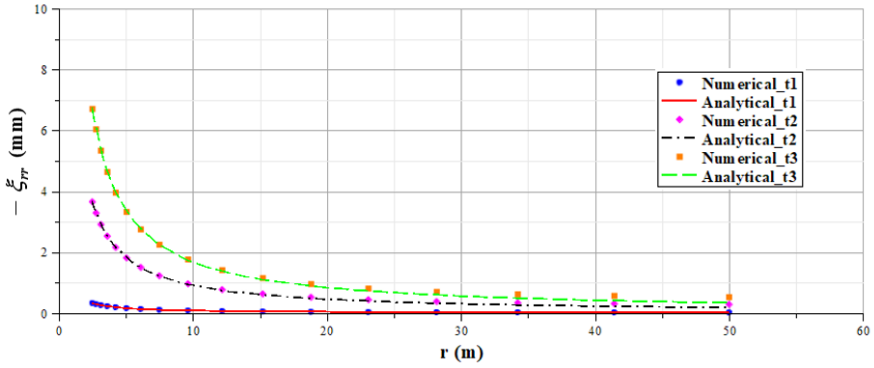

Figure 17. Comparison of radial displacements as a function of r (Burger-Maxwell)

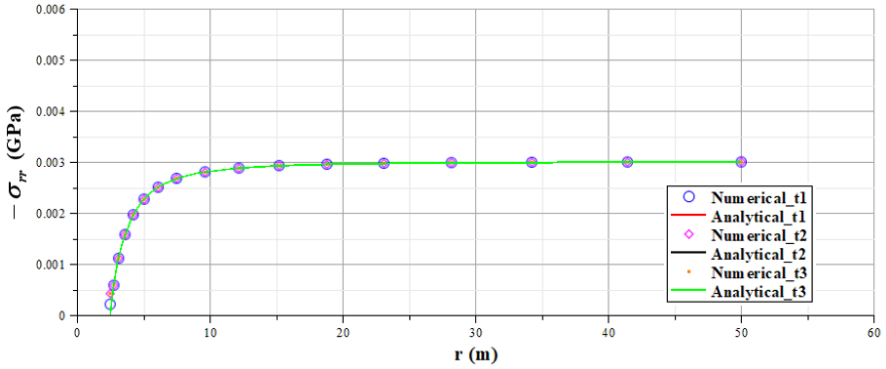

Figure 18. Comparison of radial stresses as a function of r (Burger-Maxwell)

As shown in Fig. 17-18, analytical and numerical curves present a satisfactory correspondence. It can be considered as an additional verification of correct performance of the implementation code. Despite the consistent correspondence between analytical and numerical results, boundary effects related to displacements have been observed in Fig. 17. Since boundary displacements are supposed to be zero in the discretized geometric model, it is necessary to perform future researches in order to reduce these boundary effects.

5.2 Lined circular cross-section tunnel

The hypotheses considered in this section will be the same as those used in section 5.1. In this problem, there will be a perfectly rigid lining in the tunnel cross-section. Tunnel cross-section surface presents an instantaneous radial displacement $u(R,t_0^+)$ after excavation that will be constrained with lining. Consequently, massif will exert a pressure $q(t)$ on tunnel lining (Fig. 19).

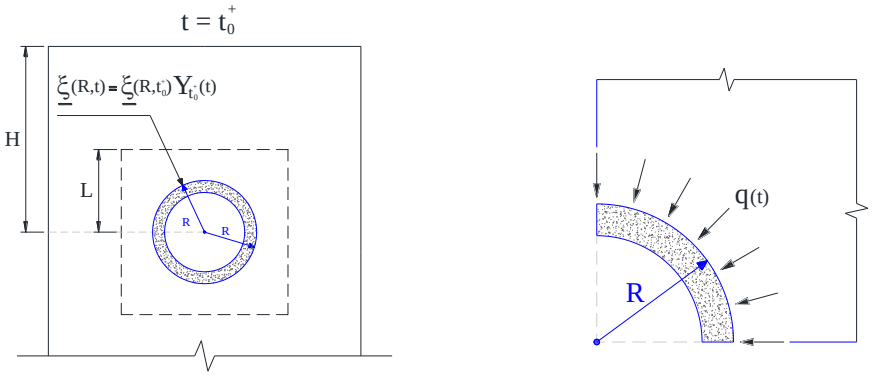

Figure 19. Displacement conditions and pressure on tunnel lining

As in section 5.1, position vector will be considered as $\underline{X} = r\,\underline{e}_r$ in polar coordinates. The problem solution involves calculation of stress and displacement fields $\left(\underline{\underline{\sigma}}(r,t), \underline{\xi}(r,t)\right)$ for $t > t_0^+$. The temporal evolution of solution fields is shown as follows:

$$\underline{\xi}(r,t) = -\frac{pR^2}{2\mu(t_0^+,t_0^+)\cdot r} Y_{t_0^+}(t)\,\underline{e}_r$$

$$\underline{\underline{\sigma}}(r,t) = \left[p\left(\frac{R^2}{r^2}\frac{\mu(t,t_0^+)}{\mu(t_0^+,t_0^+)} - 1\right)\right]\underline{e}_r \otimes \underline{e}_r + \left[-p\left(\frac{R^2}{r^2}\frac{\mu(t,t_0^+)}{\mu(t_0^+,t_0^+)} + 1\right)\right]\underline{e}_\theta \otimes \underline{e}_\theta + (-p)\underline{e}_z \otimes \underline{e}_z \tag{34}$$

where functions $\mu(t_0^+,t_0^+)$ represent viscoelastic shear modulus evaluated at times t and t_0^+,

respectively. Pressure $q(t)$ exerted by massif on tunnel lining is defined as follows:

$$q(t) = -\sigma_{rr}(R,t) = p\left(1 - \frac{\mu(t,t_0^+)}{\mu(t_0^+,t_0^+)}\right). \tag{35}$$

Concerning to the discretized geometric model, it is the same as that shown in Figure 16. In relation to Burger-Maxwell case, the analytical solution, defined in Eq. (34), will be compared with the numerical response for radial displacement $\xi_{rr}(r,t)$ and radial stress $\sigma_{rr}(r,t)$. The analysis will be performed for three different times defined in section 5.1.

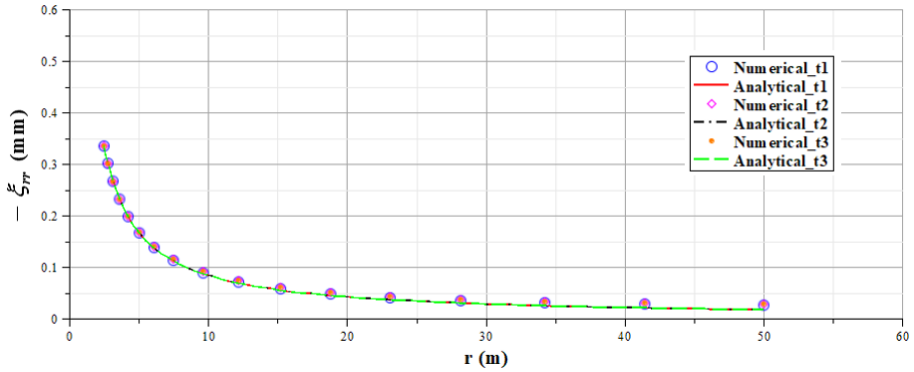

Figure 20. Comparison of radial displacements as a function of r (Burger-Maxwell)

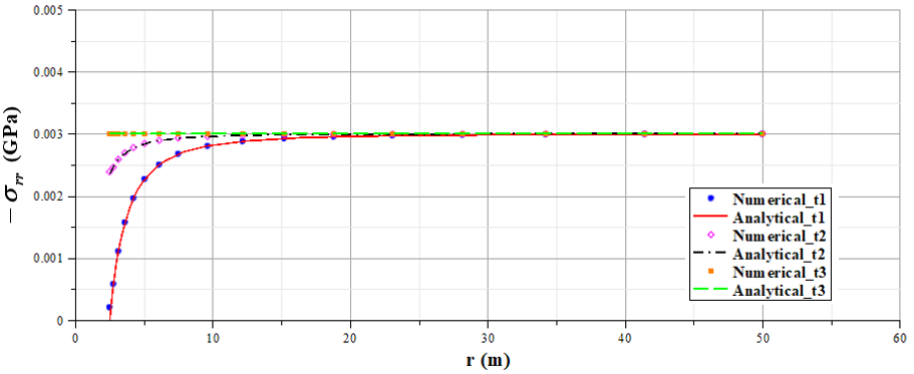

Figure 21. Comparison of radial stresses as a function of r (Burger-Maxwell)

As shown in Fig. 20-21, analytical and numerical curves present a satisfactory correspondence. This has been also an additional verification of correct performance of the implementation code. As in section 5.1, despite the consistent correspondence between analytical and numerical results, boundary effects related to displacements have been observed in Fig. 20. Therefore, it is necessary to perform future researches focused on discretized model dimensions and finite element mesh refinement in order to reduce these boundary effects.

5.3 Horseshoe cross-section tunnel

This section is focused on showing the predictive capabilities or potentialities of the computational implementation when studied complex geo-structures that don't present an analytical viscoelastic solution due to their particular geometric characteristics. Information concerning cross-section geometry, tunnel depth and specific weight of massif were obtained from Couto´s doctoral thesis [9], who performed some researches on an underground gallery located in Jagran, Pakistan. Regarding to the material viscoelastic properties, the case of delayed behavior adopted by matrix and fractures is the same as those used in sections 5.1 and 5.2. In the same way, it will be used the fracture density parameter ε, number of fractures per unit volume $\mathcal{N}$ and mechanical parameters from Tables

1 and 2. Figure 22 displays a schematic representation of the geometric model and the horseshoe cross-section.

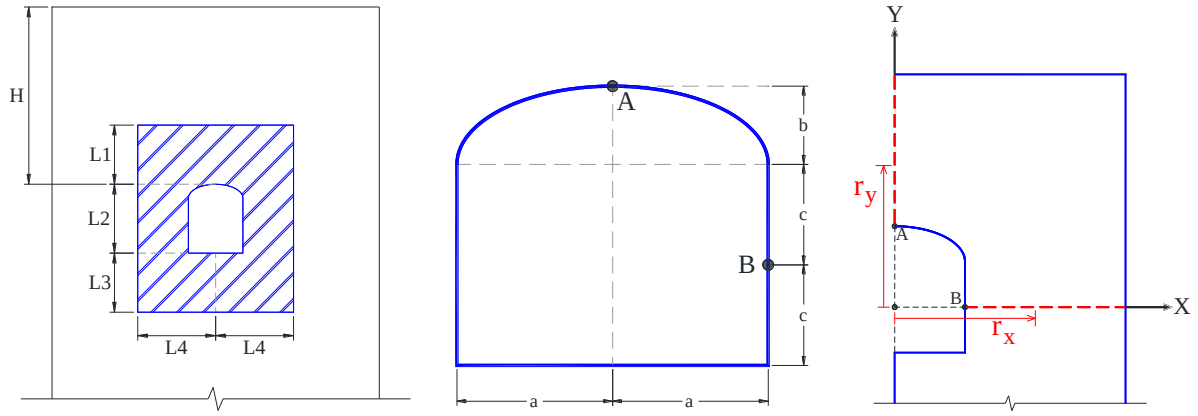

Figure 22. Geometric model dimensions and horseshoe cross-section analysis axes

Values adopted by variables shown in Fig. 22 are: $H = 270$ m., $L1 = 45.68$ m., $L2 = 16.00$ m., $L3 = 61.68$ m. and $L4 = 48.00$ m. For this paper, it was arbitrarily chosen a semielliptical geometry for tunnel vault. The values for variables of horseshoe cross-section are: $a = 6.10$ m., $b = 2.32$ m. and $c = 6.84$ m. Figure 23 illustrates the stress and strain boundary conditions, as well as the finite element mesh generated for respective analyses.

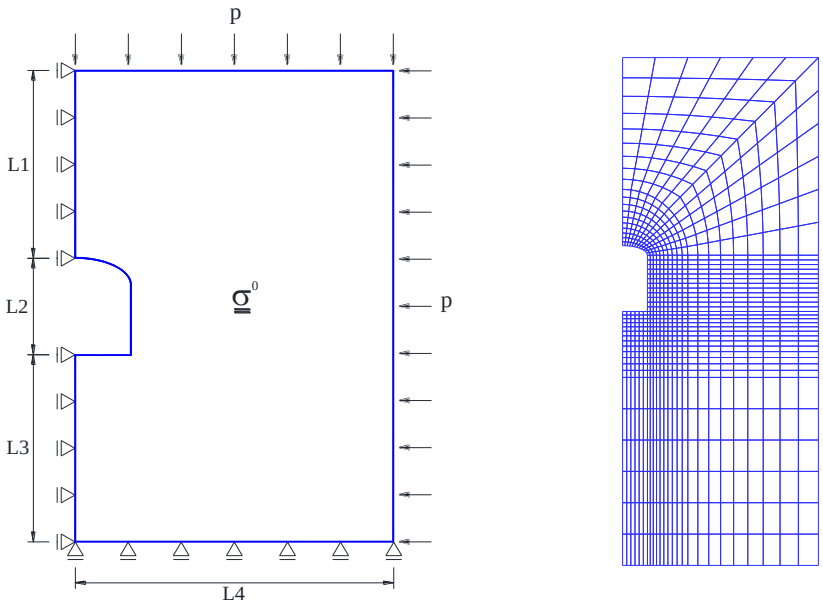

Figure 23. Boundary conditions and finite element mesh for horseshoe cross-section tunnel

It is known that $p = \gamma H$ for deep galleries, where massif specific weight is $\gamma = 25$ kN/m^3 and initial stress state before excavation is $\underline{\underline{\sigma}}^0 = -p\,\underline{\underline{1}}$.

As seen in Fig. 22, there are two marked points A and B, whose corresponding axes (Y-axis and X-axis) will be used for analysis of displacements $\left(\xi_{xx}, \xi_{yy}\right)$ and stresses $\left(\sigma_{xx}, \sigma_{yy}\right)$ as a function of distances r_x and r_y for three different times defined in section 5.1. In relation to Burger-Maxwell case, time-dependent displacements and stresses in X-axis (point B) and Y-axis (point A) are shown below.

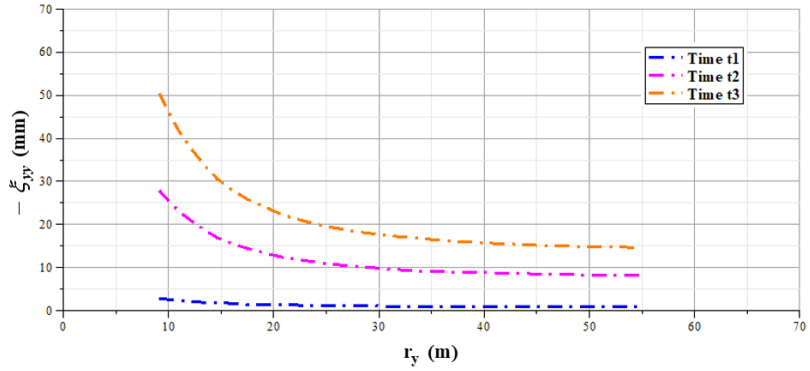

Figure 24. Vertical displacements $\xi_{yy}(r_y)$ in Y-axis (Burger-Maxwell)

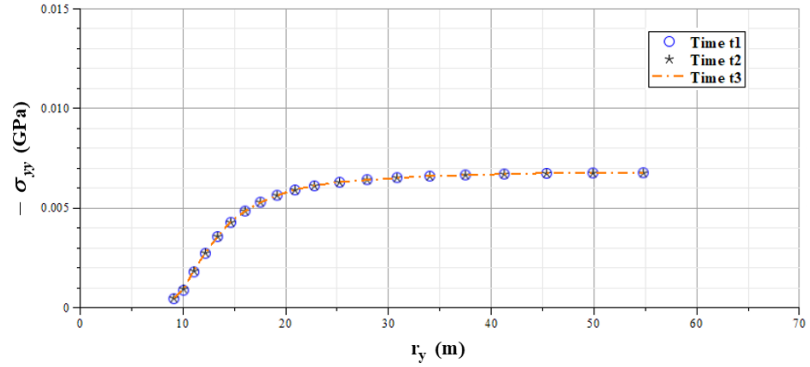

Figure 25. Vertical stresses $\sigma_{yy}(r_y)$ in Y-axis (Burger-Maxwell)

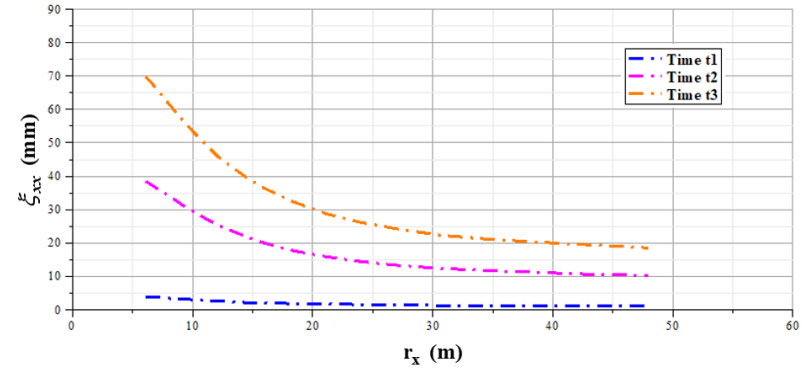

Figure 26. Horizontal displacements $\xi_{xx}(r_x)$ in X-axis (Burger-Maxwell)

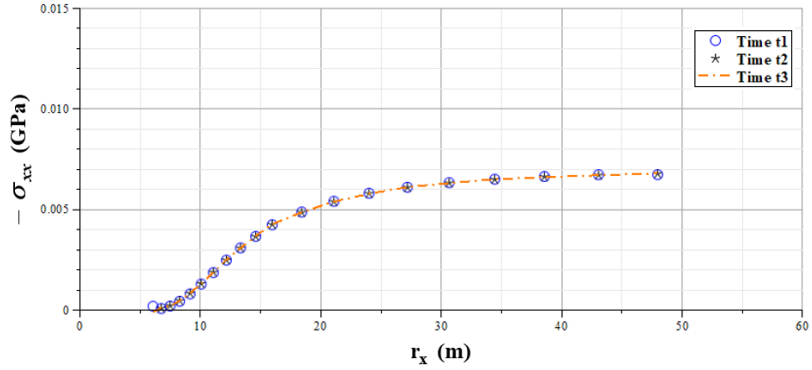

Figure 27. Horizontal stresses $\sigma_{xx}(r_x)$ in X-axis (Burger-Maxwell)

As shown in Figures 24-27, stresses and displacements present a coherent delayed behavior in the analyzed axes. As position vector moves away from cross-section surface, displacements values decrease and stresses values tend to the geostatic pressure p. Despite of boundary effects (Fig. 24 and 26) related to displacements, the implementation code works in a satisfactory way for problems that address geo-structures with presence of isotropically distributed micro-fractures

6 Conclusions

The constitutive law formulation used as theoretical basis for development of the implementation code in this paper can work with different rheological models for description of matrix and fractures delayed behavior. The general case adopts a Burger rheological model for both material constituents. The choice of these models depends on many factors, such as, for example, proposals studied in previous research works. It also depends on the possibility of using parameters obtained from laboratory tests and on the research objectives when studied viscosity effects on matrix and fractures.

The correct performance of the implementation code was verified through the examples of application shown in section 4 and through the analyses of deep circular cross-section tunnels in sections 5.1 and 5.2. This verification showed that numerical predictions have an optimal correspondence with the analytical solutions at short, intermediate and long times. In the case of deep horseshoe cross-section tunnel analysis, it was noticed a coherent delayed behavior for both displacements and stresses. The greater the distance from cross-section surface, the less the displacement given by the numerical model and stresses values tend to the geostatic pressure related to the initial stress state. In this way, the predictive capabilities of the computational tool were shown in this paper.

One of the main suggestions for extension of the present work is validation of the viscoelastic model, using the parameters identification as a first step. It would be interesting to perform tridimensional analyses with the aim to assess the predictive capabilities of the model at short, intermediate and long times by comparing numerical predictions with results obtained from laboratory tests of a specific geomaterial subjected to long-term loadings.

References

[1] S.T. Nguyen. Propagation de fissures et endommagement par microfissures dans um milieu viscoélastique linéaire non vieillissant. PhD thesis, Université Paris-Est, France, 2010.

[2] Nguyen, S. T.; L. Jeannin, L. Dormieux, F. Renard. Fracturing of viscoelastic geomaterials and application to sedimentary layered rocks. *Mechanics Research Communications*, vol. 49, pp. 50-56, 2013.

[3] C.B. Aguiar and S. Maghous. Micromechanical approach to effective viscoelastic properties of micro-fractured geomaterials. *International Journal for Numerical and Analytical Methods in Geomechanics*, vol. 42, n. 16, pp. 2018–2046, 2018.

[4] S. Maghous, L. Dormieux, D. Kondo, J.F. Shao. Micromechanics approach to poroelastic behavior of a jointed rock. *International Journal for Numerical and Analytical Methods in Geomechanics*, vol. 37, n. 2, pp. 111–129, 2013.

[5] QV. Le. Modélisation multi-échelle des matériaux viscoélastiques hétérogènes. Application à l'identification et à l'estimation du fluage propre de béton d'enceintes de centrales nucléaires. PhD thesis, Université Paris-Est, France, 2008.

[6] J. Salençon. *Mécanique des milieux continus: concepts généraux*. L'École Polytechnique (Paris), 2005.

[7] J. Salençon. *Viscoélasticité pour le Calcul des structures*. L'École Polytechnique (Paris), 2009.

[8] D. Bernaud. Tunnels profonds das les milieux viscoplastiques: approaches experimentale et numerique. PhD thesis, l´Ecole Nationale des Ponts et Chaussées, France, 1991.

[9] E.C. Couto. Um modelo tridimensional para túneis escavados em rocha reforçada por tirantes passivos. PhD thesis, Federal University of Rio Grande do Sul, Brazil, 2011.